Ⓔ

STRUCTURE OF THE DRACO DWARF SPHEROIDAL GALAXY

Slawomir Piatek

Department of Physics, New Jersey Institute of Technology, Newark, NJ 07102; piatek@physics.rutgers.edu

Carlton Pryor[1]

Department of Physics and Astronomy, Rutgers, the State University of New Jersey, 136 Frelinghuysen Road, Piscataway, NJ 08854-8019; pryor@physics.rutgers.edu

Taft E. Armandroff

National Optical Astronomy Observatory, P.O. Box 26732, Tucson, AZ 85726; tarmandroff@noao.edu

and

Edward W. Olszewski[1]

Steward Observatory, University of Arizona, 933 North Cherry Avenue, Tucson, AZ 85721-0065; eolszewski@as.arizona.edu

ABSTRACT

This article studies the structure of the Draco dwarf spheroidal galaxy, with an emphasis on the question of whether the spatial distribution of its stars has been affected by the tidal interaction with the Milky Way, using R- and V-band CCD photometry for 11 fields. The article reports coordinates for the center, a position angle of the major axis, and the ellipticity. It also reports the results of searches for asymmetries in the structure of Draco. These results and searches for a '' break '' in the radial profile and for the presence of principal sequences of Draco in a color-magnitude diagram for regions more than $50'$ from the center yield no evidence that tidal forces from the Milky Way have affected the structure of Draco.

Key words: galaxies: dwarf — galaxies: individual (Draco) — galaxies: stellar content — galaxies: structure — Local Group

On-line material: machine-readable tables

1. INTRODUCTION

This article studies the structure of the Draco dwarf spheroidal (dSph) galaxy. The dSph galaxies are characterized by small size, low luminosity, low surface brightness, and old- to intermediate-age stellar populations. The Local Group dSph's are clustered around and appear to be gravitationally bound to the much more luminous spiral galaxies (see the review by van den Bergh 2000). Draco, together with at least eight other dSph's, is a satellite galaxy of the Milky Way. Draco is 80 ± 7 kpc from the Sun (Aparicio, Carrera, & Martínez-Delgado 2001, hereafter ACMD), and, although its tangential velocity is not known, the measured radial velocity, corrected for solar motion, -98 km s^{-1} (Olszewski, Aaronson, & Hill 1995; Armandroff, Olszewski, & Pryor 1995), implies that Draco is currently approaching the Milky Way.

Even though the masses of dSph's are small in comparison with those of luminous spiral and elliptical galaxies, many of their mass-to-light ratios (M/L) are very large (Aaronson 1983; Mateo 1998). For example, the M/L_V of Draco is 90, assuming that mass follows light (Armandroff et al. 1995), and 340–610, by using more realistic models (Kleyna et al. 2001)—this is the highest measured value among the Galactic dSph's. The presence of nonluminous or dark matter is present in Draco is the most direct interpretation of its large M/L. However, several authors have proposed alternative explanations for the large measured M/L values of dSph's in general and Draco in particular.

These explanations either invoke a modification of the laws of gravity (MOND; Milgrom 1983) or require that the dSph be far from virial equilibrium because of its interaction with the Galactic tidal field.

Kuhn & Miller (1989) and Kuhn (1993) proposed that a resonance between the orbital frequency and the frequency of internal collective oscillation modes of a dSph drives the dSph far from virial equilibrium. In this picture, a dSph with a large measured M/L is a gravitationally unbound stellar system that does not dissipate quickly because the stars are on Galactic orbits that keep them together. However, Sellwood & Pryor (1998) show through numerical simulations that only a stellar system with even lower central concentration than those of the observed dSph's has collective modes that are not strongly damped and even in such a system these modes are not excited by coupling to the orbital motion. Oh, Lin, & Aarseth (1995) modeled weak but nonresonant tidal interactions between the Galaxy and a dSph that led to the formation of tidal debris around the dSph but did not increase the velocity dispersion and M/L to the values measured for real dSph's.

Piatek & Pryor (1995) examined whether a single strong tidal shock that disrupts a dSph can produce the large velocity dispersion and M/L values measured for real dSph's. This study found that such tidal interactions do not increase the velocity dispersion, but instead they produce a large velocity gradient along the major axis. Kroupa (1997) studied models in which the tidal debris from the dSph is aligned along the line of sight, in which case the velocity gradient masquerades as a large velocity dispersion. These models require that the dSph's with large measured M/L values be on nearly radial orbits. They also predict vertical broadening of the principal sequences, such as the horizon-

tal branch, in the color-magnitude diagram (Klessen & Kroupa 1998; Klessen & Zhao 2002).

The presence of tidal debris around a dSph does not prove that their measured M/L values have been raised by tidal interactions. For example, Grillmair et al. (1995) and Leon, Meylan, & Combes (2000) detected tidal debris around globular clusters, which have measured M/L_V values of 1–3 (Pryor & Meylan 1993) that agree well with those expected from their stellar populations. However, because the spatial extent and the surface density of tidal debris depends on the mass distribution, intrinsic M/L, and orbital elements of the dSph, along with the Galactic potential, detecting and quantifying the tidal debris can yield information about these quantities (e.g., Kuhn 1993; Moore 1996; Johnston et al. 1999a, 1999c). In addition, deriving the amount and distribution of dark matter in a dSph by using the kinematics of a tracer population requires measurements of the projected density profile of that population. Limits on the central density of dark matter are particularly sensitive to the shape of the profile at large radii (Pryor 1994).

Irwin & Hatzidimitriou (1995, hereafter IH; see the references therein for earlier work) derived radial profiles and structural parameters for most of the Galactic dSph's by using star counts from Palomar and UK Schmidt telescope plates. IH determined limiting, or tidal, radii for a dSph by fitting single-component isotropic King models to its profile. They noted that in many cases the dSph has a profile that is above the fitted King model at large radii, which they interpret as evidence for "extratidal" stars. Many subsequent studies have interpreted the IH tidal radius as the boundary between gravitationally bound and unbound populations. However, the two-body relaxation time of every dSph is longer than its age (Webbink 1985), and so there is no reason that the dSph must resemble a King model. Indeed, it is possible to find many equilibrium models that fit perfectly almost any projected density and projected velocity dispersion profile (Dejonghe & Merritt 1992).

Several groups have recently studied the structure of the Draco dSph. Smith, Kuhn, & Hawley (1997) detected apparent stars of Draco extending up to $3°$ east of the center—far beyond the $28\farcm3$ tidal radius determined by IH. They interpret these stars as a tidally unbound population. In contrast, Piatek et al. (2001, hereafter P01) found evidence for Draco stars beyond the IH tidal boundary, though only weak evidence for stars with distances as large as $1°$. Odenkirchen et al. (2001a, hereafter Od01) studied the morphology of Draco by using Sloan Digital Sky Survey data for a wide region around the galaxy. They derived a limiting (or tidal) radius for Draco of $49\farcm5$, which is 75% greater than the IH value. Thus, they argue that the stars of Draco detected by P01 are within the tidal boundary and therefore are gravitationally bound to Draco. The Od01 upper limit for the surface density of Draco stars beyond their limiting radius is a factor of 10 lower than the surface density detected by Smith et al. (1997). Od01 argue that this detection resulted from an incorrectly estimated background. Interestingly, they also note that an exponential model fits their data better than a King model, so the actual existence of a limiting radius is called into doubt. Finally, ACMD derive a radial profile of Draco that is in broad agreement with that of Od01.

The large discrepancy in the values for the limiting radius of Draco obtained by IH and Od01 underscores the large uncertainties in this fitted parameter. Since the dynamics of the tidal debris is decoupled from the internal dynamics of the dSph, the surface density profile of the tidal debris and that of the dSph should have different spatial structure. Johnston, Sigurdsson, & Hernquist (1999b) performed numerical experiments that show that a robust indicator of tidal debris around a dSph is the presence of an abrupt change in the local power-law index of the radial surface density profile of a dSph—a "break" in the profile. The presence of tidal debris causes the surface density to decrease less steeply in the outer regions of a dSph. Note, however, that Kroupa (1997) argues that a profile resembling that of a real dSph may be produced by an unbound population of stars. It seems therefore that the limiting radius of a dSph is not a trustworthy representative of the tidal boundary of a dSph.

In this article we report the results of a study of the structure of Draco, based on the R- and V-band photometric data for 11 fields in and around Draco. We derive such structural parameters as the center, position angle, and ellipticity. In addition, we search for tidal debris by using methods based on color-magnitude diagrams, the radial profile of the surface density, and the shape of isopleths of a map of the surface density. We compare our results with those from the existing studies of Draco.

Section 2 describes the data and its reduction. Section 3 presents the color-magnitude diagrams (CMDs) for the new N1 and S1 fields, describes the procedure for discriminating between nonmembers and possible members of Draco, based on location in the CMD and image morphology, and compares the sample of possible members of Draco from this paper with those from ACMD and Od01. Section 4 derives model-independent structural parameters of Draco and a map of the projected density of the galaxy. The section also comments on the reality of asymmetries in the projected density map. Section 5 summarizes and discusses our main results.

2. DATA ACQUISITION AND REDUCTION

The data consist of R- and V-band photometry of objects from 11 fields that are located in and around the Draco galaxy. Photometry for nine of these fields is the same as those that P01 used in their study. The two additional fields, N1 and S1, are adjacent to the central C0 field of P01 in the north and south directions, respectively, and extend beyond the tidal boundary along the minor axis. These additional fields were imaged with the KPNO 0.9 m telescope using the 2048×2048 T2KA CCD chip (see P01 for more details). There is a $0\farcm55$ overlap between the N1 and C0 fields, while there is a $1\farcm85$ gap between S1 and C0. The N1 and S1 fields were taken under nonphotometric conditions, and so we obtained two tie fields centered roughly halfway between the N1 and C0 and S1 and C0 fields. Table 1 lists the basic information about the N1 and S1 fields and their corresponding tie fields. This table supplements Table 1 in P01, which lists this information for the other nine fields. Columns (1) and (2) list the name of the field and the date of data acquisition. Columns (3)–(7) list the coordinates of the center of the field, first in the equatorial system and then in the Galactic system. Columns (7) and (8) list the total exposure times for the V and R bands, respectively, and columns

FIELD (1)	DATE (2)	R.A. (J2000.0) (3)	DECL. (J2000.0) (4)	l (deg) (5)	b (deg) (6)	T_{exp} (s) V (7)	R (8)	FWHM (pixels) V (9)	R (10)
N1.............	1992 May 28	17 20 01.18	58 17 12.52	86.8208	34.7227	3×1700	4×2000	2.40 ± 0.18	3.37 ± 0.33
N1(tie)	1992 Jun 2	17 20 01.30	58 06 00.52	86.5942	34.7345	1×100	1×100	...	...
S1..............	1992 May 30	17 20 01.65	57 31 42.52	85.8996	34.7683	3×1700	3×1600	2.18 ± 0.19	2.19 ± 0.18
S1(tie)	1992 Jun 2	17 20 01.54	57 43 09.52	86.1315	34.7575	1×100	1×100	...	...

NOTE.—Units of right ascension are hours, minutes, and seconds, and units of declination are degrees, arcminutes, and arcseconds.

(9) and (10) list the average value and rms scatter around the average for the FWHM of the stellar images in the V- and R-band frames, respectively. The FWHMs were measured in the same way as those in P01.

The data for the N1 and S1 fields have a more variable FWHM than the majority of the P01 fields because they were taken before the installation of the two-element field flattener on the 0.9 m telescope. The N1 R-band data have the worst seeing of any of our data. The N1 V-band data were taken through clouds, and they have less total exposure time than our other V-band data. We discuss the impact of these deficiencies on our results in §§ 2.2 and 3.2.

The instrumental magnitudes of objects in the N1 and S1 fields were obtained by the same method described in P01-DAOPHOT (Stetson 1987, 1992, 1994) photometry of combined frames. The tie frames determine the transformation between the instrumental and standard magnitudes. Because the tie frames were also taken under nonphotometric conditions we use them to transform N1 and S1 to the same photometric system as C0. To do so, we use the following procedure: (1) determine aperture magnitudes for objects in the tie frame by using a 6 pixel aperture radius, (2) match the objects that are common to the C0 and tie frames, (3) by using these objects with their standard magnitudes measured in C0, derive a photometric transformation which converts aperture magnitudes to standard magnitudes in the tie frame, (4) match objects common to the science and tie frames, and (5) by using these objects, derive a photometric transformation that converts instrumental magnitudes in the science frame to standard magnitudes.

Tables 2A–2B list the standard R- and V-band photometry for the N1 and S1 fields, respectively. In these tables columns (1)–(5) list, respectively, the ID, x and y coordinates on the R frame, and α(J2000.0) and δ(J2000.0) for an object. The equatorial coordinates come from plate solutions based on positions for stars in the USNO-A2.0 catalog (Monet et al. 1998), by using a recipe developed by Paul Harding (2001, private communication). Columns (6) and (7) list the R-band magnitude followed by its uncertainty, σ_R. Columns (8) and (9) list the same for the V band. Columns (10) and (11) list the average CHI and SHARP values (described in § 3.2).

2.1. Comparison of Photometry from Overlapping Fields

The regions of overlap between the N1 and C0 fields and between the S1 and SE1 fields allow a comparison of the magnitudes for the objects in common. Figure 1a plots the magnitude difference, $\Delta R \equiv R_{N1} - R_{C0}$, versus R_{N1} for the 47 objects that are common to the N1 and C0 fields and are matched to within a 0″.69 radius—which is equivalent to about 1 pixel. Similarly, Figure 1b plots the magnitude difference for the V band.

The unweighted mean of ΔR is -0.061 ± 0.018, where the uncertainty is estimated from the rms scatter around the mean. This calculation excludes the three brightest objects in the sample, one of which is out of the plot to the left and all of which are saturated in the N1 image, the two dimmest objects, which have large uncertainties, and the two objects near $R = 20$ with positive ΔR, whose R- and V-band photometry suggest are RR Lyrae variables. The offset between the zero points of the two fields is likely due to the poor focus near the edges of the C0 frame. However, our calibration procedure ensures that the average zero-point shift between the two fields is zero.

The unweighted mean of ΔV is -0.083 ± 0.026. This calculation excludes the two brightest objects, one of which is out of the plot to the left and both of which are saturated in the C0 frame, objects dimmer than $V = 23$, which have

TABLE 2A
R AND V PHOTOMETRY OF DRACO: N1 FIELD

Star (1)	X (pixel) (2)	Y (pixel) (3)	R.A. (J2000.0) (4)	Decl. (J2000.0) (5)	R (6)	σ_R (7)	V (8)	σ_V (9)	CHI (10)	SHARP (11)
1........	992.939	3.848	17 19 59.94	58 29 28.68	18.7966	0.0130	20.1291	0.2470	2.4500	-0.1885
2........	2021.190	4.042	17 21 30.29	58 29 34.74	22.8216	0.1420	24.6568	1.3110	0.8000	-0.2050
3........	1826.177	4.789	17 21 13.16	58 29 33.35	24.7650	1.1390	23.1011	0.1690	0.6000	0.8010
4........	461.167	5.034	17 19 13.23	58 29 23.11	24.2232	1.0220	23.7379	0.3310	0.8350	4.9850
5........	828.858	5.066	17 19 45.53	58 29 26.49	23.1941	0.2410	23.0870	0.1550	0.5700	-0.4865

NOTE.—Tables 2A–2B are presented in their entirety in the electronic edition of the Astronomical Journal. A portion is shown here for guidance regarding their form and content.
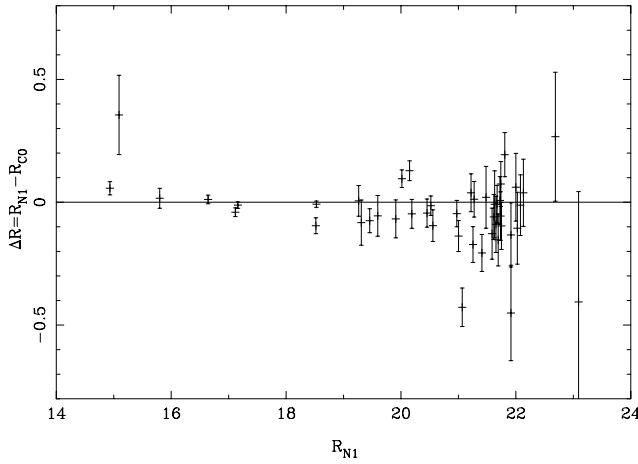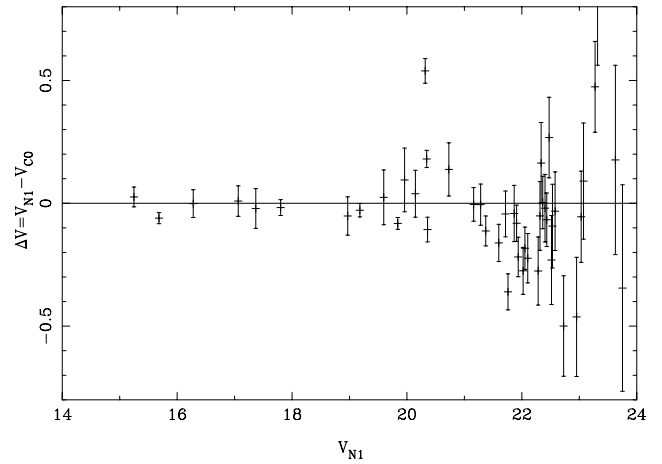
FIG. 1a

FIG. 1b

FIG. 1.—(a) Comparison of the R-band magnitudes for the 47 objects common to the N1 and C0 fields. (b) Same as (a), but for the V band.

large uncertainties, and the same two likely RR Lyrae varia-bles excluded from the calculation of the mean ΔR. Visual inspection of Figure 1b shows that the mean ΔV for the objects brighter than about $V = 21$ is closer to zero than the mean value calculated above, arguing that there is no large zero-point difference for the V-band photometry.

Figure 2a plots the magnitude difference, $\Delta R \equiv R_{S1} - R_{SE1}$, versus R_{S1} for the 115 objects common to the S1 and SE1 fields. Similarly, Figure 2b plots the magnitude differ-ence for the V band. The unweighted mean, ΔR is 0.058 ± 0.013. This calculation excludes the brightest object, which is saturated, and objects fainter than $R = 23$, which have large uncertainties. Again, this difference is likely due to the variable focus across the S1 field. Excluding the brightest object and objects fainter than $V = 23$, the unweighted mean, ΔV, is -0.027 ± 0.031. The plots and mean magnitude differences for both the R- and V-band photometry show that the zero points of the S1 and SE1 fields are in acceptable agreement.

2.2. Completeness

The variation of the photometric completeness with posi-tion distorts the measured structure of a stellar system.

Weighting each object by the inverse of the completeness estimated for its magnitude and position will reduce the dis-tortion of the structure. We perform numerical experiments to determine the level of completeness as a function of mag-nitude and position within a field for all our fields.

In an experiment, we add artificial stars to both the R- and V-band frames by using a grid that places a star at the same location on the sky. The spacing of the grid is 8 pixels (5″.5) in both directions, which results in adding about 65,000 artificial stars to each field. The addition of such a large number of artificial stars in a single experiment does not affect the crowding of the artificial stars because the stars are arranged on a grid and thus do not overlap each other. An artificial star has the point-spread function that was derived for its frame during the photometric reduction process.

We perform five completeness experiments for every field, reducing the R- and V-band frames together in the same way as the real data. The artificial stars in a given experi-ment and frame have the same magnitude and color, chosen from the isochrone described in P01. The magnitude and color pairs used in the five experiments are $(R, V-R) = (21.1, 0.406)$, $(21.6, 0.395)$, $(22.1, 0.368)$, $(22.6, 0.288)$, and $(23.1, 0.257)$. An artificial star is counted
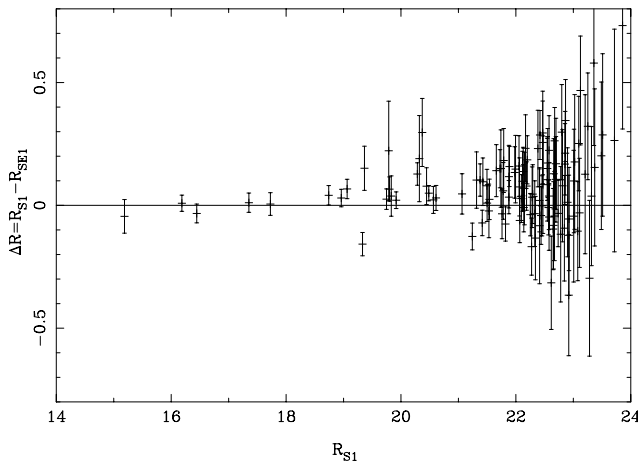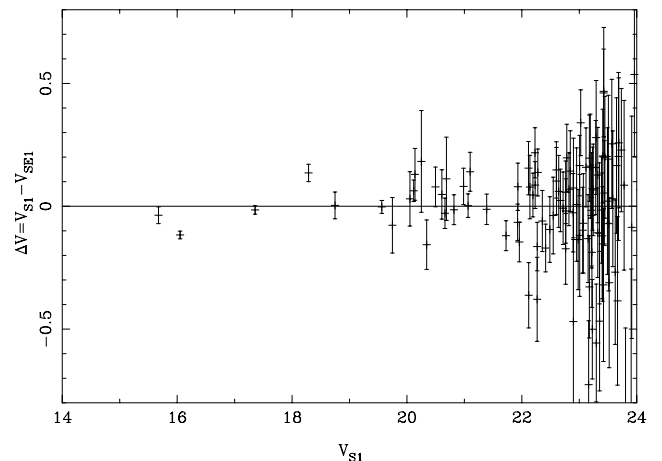

FIG. 2a

FIG. 2b

FIG. 2.—(a) Comparison of the R-band magnitudes for the 115 objects common to the S1 and SE1 fields. (b) Same as (a), but for the V band.

as recovered if it is measured in both frames and its position is within one-half pixel of its input position, irrespective of how the recovered magnitude compares with the input magnitude.

The completeness must be averaged over a region larger than the spacing of the grid of artificial stars and large enough to contain a fair sample of the local surface density of objects. In addition, this region should be smaller than the size of the structure in Draco. We adopt a circular window with a radius of 200 pixels to smooth out the effects of saturated stars and their charge overflow columns, which create the largest regions with big fluctuations in the surface density of objects. Using a weighted average in which the weight varies with distance, r, from the center of the window as $[1 - (r/200 \text{ pixels})^2]^2$ yields a completeness that changes smoothly with position. The C0 field has the largest number of saturated stars and the steepest density gradients. Thus, in this field only, the estimates of both the completeness and the surface density exclude regions around some of the brightest stars. See § 4.2 for more details.

Placing the center of the window at points with a spacing of roughly 40 pixels in both directions yields an array of average completenesses. There are five arrays per field, one for each magnitude and color pair of artificial stars. An object with $16.4 < R < 22.6$ has a completeness calculated by bicubic spline interpolation in position and linear interpolation in magnitude. Objects brighter than $R = 16.4$ have a completeness of 1.0, whereas objects dimmer than $R = 22.6$ are excluded from the analysis.

Figure 3 plots the ratio of the total number of recovered artificial stars to the number added versus magnitude for each of our 11 fields. The C0 and N1 fields are significantly shallower than the others. The lower completeness of C0 at $R \leq 22.1$ is due to the larger number of bright saturated stars in this field. The C0, N1, S1, and E1 fields, imaged before the installation of the field flattener, show a larger and more systematic variation of the completeness within a field than the rest of the fields. The completeness decreases with increasing distance from the center in the C0 and E1 fields. The difference in completeness between the center and edge can be as large as 0.4 when the completeness is changing most rapidly with magnitude (see Fig. 3). In contrast, N1 and S1 have a larger completeness at the edge than in the center. The largest differences are similar to those for C0 and E1. Only within small regions near two corners of field C0 does the completeness fall below 0.5 at $R = 22.6$.

The completeness simulations show that the errors in the magnitude and color of a recovered star become rapidly larger as the input magnitude approaches the limiting magnitude of the data. Because of this effect, a Draco star can appear far from the principal sequence of Draco in the CMD, and thus, not be counted as a member of the galaxy. Likewise, a field star or galaxy can be scattered close to the principal sequence of Draco and be counted as a member. Measuring this effect would require artificial-star experiments that added objects throughout the CMD. Such experiments are difficult to implement because they require knowing the true distribution of stars in the CMD, and so they have not been done in any study of the structure of a dSph. This effect is most important for the weak C0 and N1 fields, and §§ 4.2 and 4.6 discuss the impact of this effect on our results. Wide-field CCD cameras are now available on many large telescopes; thus, obtaining higher quality data is a better approach to this problem than performing more elaborate completeness experiments.

2.3. *Tangent Plane Projection*

Expressing the positions of objects in a single standard coordinate system simplifies the study of the structure of a stellar system. Therefore, we convert positions of objects measured in pixels within each frame into offsets in arcminutes from a chosen center by performing a tangent plane projection. The offsets are with respect to equatorial position $17^h 20^m 18^s\!.66$ and $57°55'5''\!.55$ (J2000.0), which corresponds to the center of gravity of Draco determined by IH. In our standard system, the X-offset increases eastward and the Y-offset increases northward.

3. COLOR-MAGNITUDE DIAGRAMS

Figure 4 (*top*) shows a CMD for all objects in the N1 field. Figure 4 (*bottom*) is the same for the S1 field. The magnitudes and colors of the objects in both panels are not corrected for either reddening or extinction.

The CMDs for the N1 and S1 fields show blue stars on the horizontal branch of Draco near $R = 20$ and the lower red giant branch (RGB) stars at about $V - R = 0.3$ and $20 \lesssim R \lesssim 23$. This is expected since part of both fields are within the tidal boundary of Draco.

3.1. *Reddening and Extinction*

The variation of extinction within and between our fields can also distort the measured structure of a stellar system. To reduce the impact of this variation we determine average reddening and extinctions for entire fields by using the prescription of Schlegel, Finkbeiner, & Davis (1998). The reddenings for the N1 and S1 fields are 0.030 and 0.029, respectively. These yield V- and R-band extinctions of 0.099 and 0.080, respectively, for the N1 field and 0.097 and 0.078, respectively, for the S1 field. Even after correcting for reddening and extinction, small differences in our photometric zero points remain, as evidenced by differences in the color of the blue edge of the distribution of field stars in the CMD, measured as described in P01. This color is 0.234 for the N1 field and 0.242 for the S1 field.
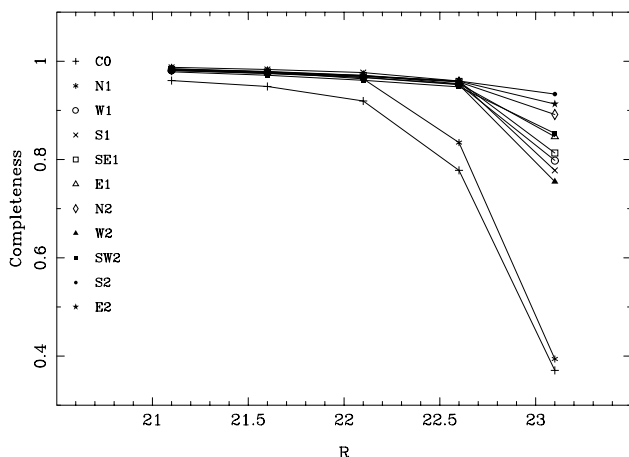

FIG. 3.—Average completeness as a function of magnitude for the 11 fields. Each point is the ratio of the number of recovered to the number of added artificial stars.
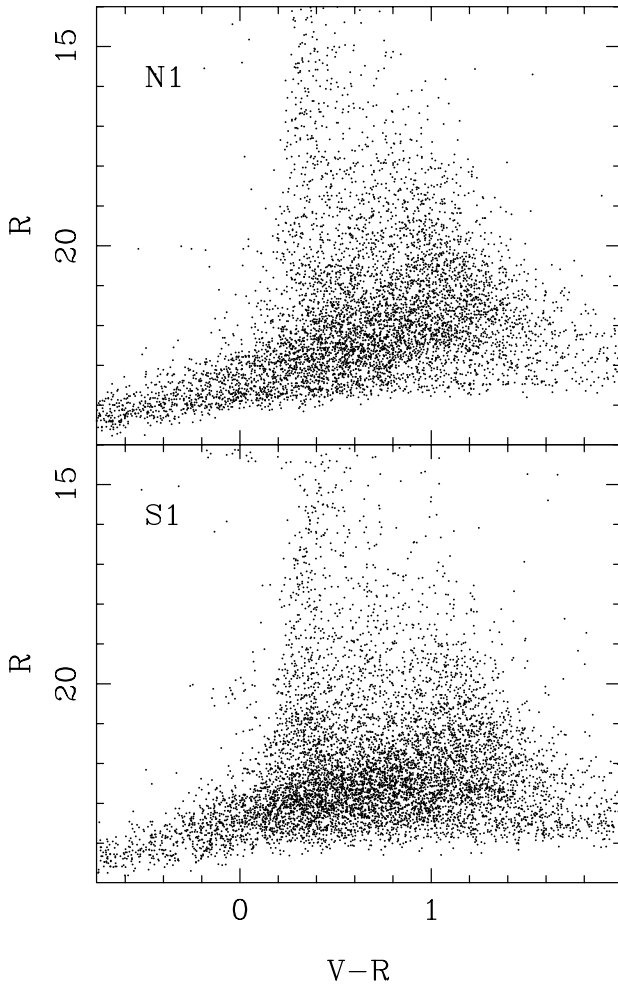
FIG. 4.—Color-magnitude diagrams for N1 (*top*) and S1 (*bottom*). Only objects with CHI values less than 5 and SHARP values within the limits shown in Fig. 5 appear in these diagrams.

3.2. *Selecting Samples Using* CMD, SHARP, *and* CHI *Criteria*

The objects in our fields consist of stars and galaxies. The former are both Galactic foreground stars and members of Draco. The structure of Draco can best be measured using a sample of objects containing a large number of Draco stars while at the same time containing the smallest number of field stars and galaxies. The lines in Figure 5 (*left*) outline the region in the CMD where Draco stars are present. The selection of this region is discussed below. The lines in Figure 5 (*right*) outline the region where stars are found in the diagram that plots SHARP value versus magnitude. A large positive value of the SHARP index calculated by the DAO-PHOT package indicates an object that is more extended than the point-spread function, which is likely a galaxy. DAOPHOT also calculates CHI, a measure of the quality of the point-spread function fit. Values larger than 5.0 occur for galaxies and spurious objects such as pixels with charge overflow. The remainder of this paper uses the sample of objects that likely are stars on the basis of their CHI and SHARP values and separates these into samples of likely members (the "in" sample) and likely nonmembers (the "out" sample) of Draco on the basis of their position in the CMD.

Figure 5 plots every second object from the C0 field and every tenth object from the other fields to show clearly both the Draco sequences and the distribution of field stars and galaxies. The width of the region outlining the RGB of Draco in Figure 5 (*left*) is proportional to the uncertainty in color for $R < 21.6$. The width is about $\pm 2\,\sigma_{V-R}$, which is narrower than the $\pm 3\,\sigma_{V-R}$ used in P01. The narrower width increases the fraction of Draco members in the outlined region. For $R > 21.6$ the outlined region does not extend further to the red with the increasing uncertainty in color to avoid the large number of field stars. However, the region extends even further to the blue to include possible blue stragglers of Draco. The region of allowed SHARP values in Figure 5 (*right*) is 40% wider than that in P01 to accommodate the more variable focus of the C0, N1, S1, and E1 fields.

The artificial-star simulations described in § 2.2 show that the large photometric uncertainties of the faint objects will scatter them both into and out of the "in" and "out" samples. This effect can alter the measured structure of Draco because the distribution of objects in the CMD is not the same in all our fields. For example, our C0 and N1 fields are shallower than the others. As discussed in § 2.2, we do correct our data for completeness but we have chosen not to correct for this scattering effect.

3.3. *Background Surface Density*

We determine the background surface density of the "in" and "out" samples using the most distant fields: N2, E2, S2, SW2, and W2, which are about $1°$ from the center of Draco (see Fig. 1 in P01). The weighted mean surface density of the background for the "in" sample is 1.446 ± 0.026 arcmin^{-2}. The weight for each surface density is the inverse of the square of the sampling uncertainty. The χ^2 of the scatter around the mean is 4.96 for three degrees of freedom (the S2 and SW2 fields were combined into one since they overlap). The probability of exceeding this value by chance is 0.17, so there is no evidence for more variability than expected from counting statistics and the stated uncertainty in the mean is realistic. For the "out" sample, the χ^2 of the scatter around the weighted mean is 22.8 and the probability of exceeding this by chance is 4.4×10^{-5}. The clustering of galaxies causes the larger variability of the surface density compared with that expected from the sample size (see the detailed discussion in P01). Thus, for the "out" sample we adopt an unweighted average background of 3.91 ± 0.12 arcmin^{-2}, where the uncertainty is based on the scatter around the mean.

3.4. *Comparison with Other Samples*

The current paper is one of several that have recently studied the structure of Draco by using star counts. This section briefly compares our "in" sample with the corresponding samples from ACMD and Od01. The goal is to assess how well these samples determine the structure of Draco.

The "in" sample in this paper is intermediate in both limiting magnitude and radial extent compared with those in ACMD and Od01. Its limiting magnitude is about 2.6 mag below the level of the horizontal branch compared with about 4.0 mag below for ACMD and 1.8 mag below for Od01. The Od01 sample has complete azimuthal coverage to a distance of $2°$ from the center of Draco, whereas the
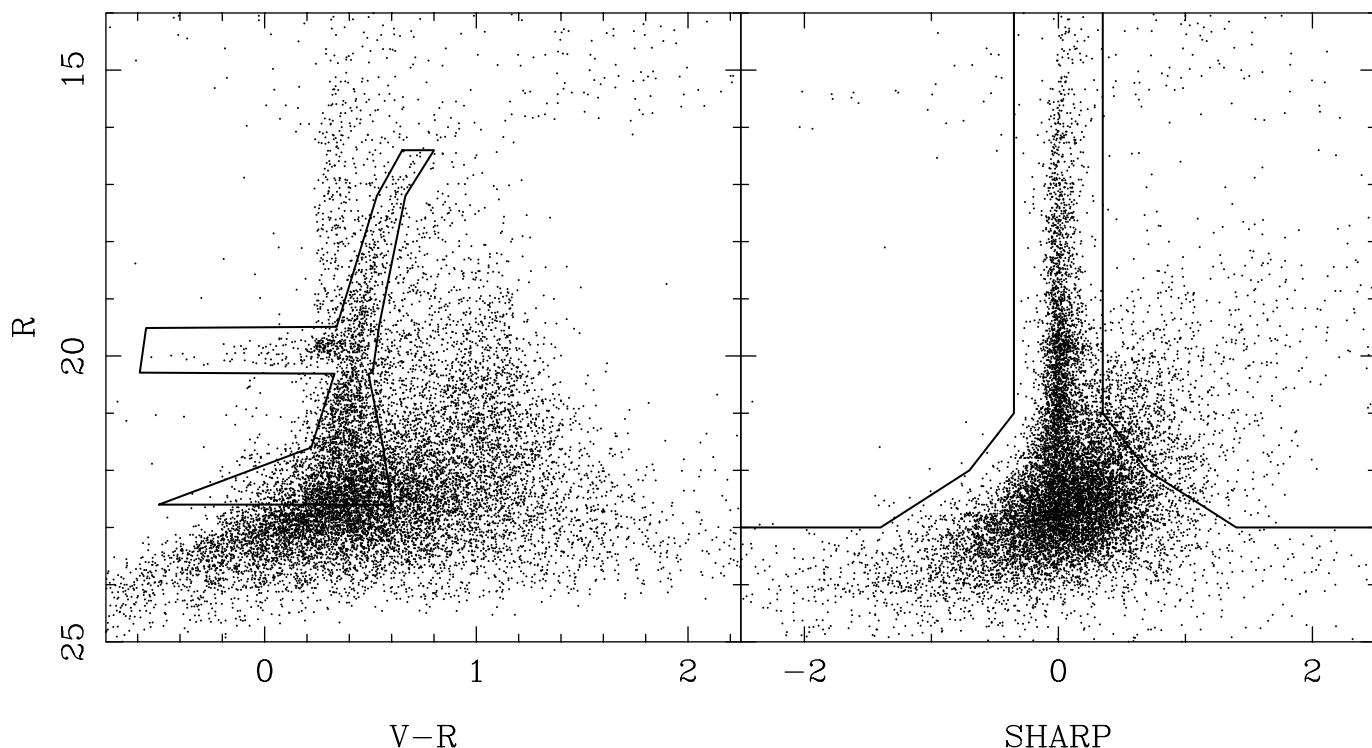
FIG. 5.—*Left*: Color-magnitude diagram showing every second object from the C0 field and every tenth object from the other 10 fields. The solid contours outline the principal sequences of Draco. *Right*: *R*-band magnitude vs. SHARP for the same sample of objects as that on the left. The solid lines represent the SHARP limits we adopt to discriminate between stars and galaxies. The objects within the lines are likely to be stars, and those outside are likely to be galaxies or spurious objects. The two panels define the "in" and "out" samples: the "in" sample consists of objects within the outlined regions in both panels, whereas the "out" sample consists of those that are outside the outlined region in the left (and brighter than $R = 22.6$) but within the outlined region in the right.

"in" sample has six inner fields extending to about $50'$ from the center and five background fields about $1°$ from the center (see Fig. 1 in P01). The ACMD sample has three fields extending to about $50'$ from the center of Draco.

The central surface density and its ratio to the background surface density far from the center are two of the best measures of the quality of a sample for determining the structure of Draco. The central surface density of the "in" sample (presented in § 4.6) is half that of the ACMD main-sequence sample but it is about 3 times that of the Od01 sample. The ratio of the central and background surface densities for the "in" sample is 3–5 times smaller than those of the ACMD and Od01 samples, reflecting the better discrimination against nonmembers in the CMD allowed by the homogenous photometry in Od01 and by the deeper photometry in ACMD. These comparisons show that the "in" sample is better than the Od01 sample for studying the inner regions of Draco. The ACMD sample would be better still; however, this work is focused on the stellar populations rather than on the structure of Draco.

4. MODEL-INDEPENDENT STRUCTURE

This section examines the structure of Draco without assuming a parametric model. It first discusses the derivation of a smooth surface density map for objects from our data by using an adaptive kernel. Discussions of a contour plot of the surface density map and of estimates of the center of the galaxy and of the position angle of its major axis follow. The section ends by discussing the centers, position

angles, and ellipticities resulting from fitting ellipses to the smooth surface density map.

4.1. *Adaptive Kernel Estimate of the Smooth Surface Density*

The construction of a surface density map from the positions of objects on the sky requires smoothing. Kernel estimators are commonly used for this purpose (e.g., Silverman 1986). For systems with large variations in the surface density a kernel whose width decreases as the density increases—an adaptive kernel—recovers the maximum amount of information.

We use a parabolic kernel to construct the smoothed density map for Draco on a grid of points following the methods outlined in Silverman (1986). A kernel with a fixed width creates a "pilot" density estimate. The final surface density map uses an adaptive kernel whose width is inversely proportional to the square root of the pilot density at each grid point. This procedure keeps the number of objects contributing to each kernel area approximately constant.

The construction of the surface density map from our data is complicated by the incomplete areal coverage of our fields. There are swaths of missing data northwest, southwest, and northeast from the galaxy and small gaps in the data between the C0 and W1 and C0 and S1 fields. There are also numerous holes in the data due to bright and saturated stars. We generate artificial data to fill in the empty regions within an area of $120'$ by $120'$ centered on Draco. Most of the empty regions, shown in white in Figure 6, have
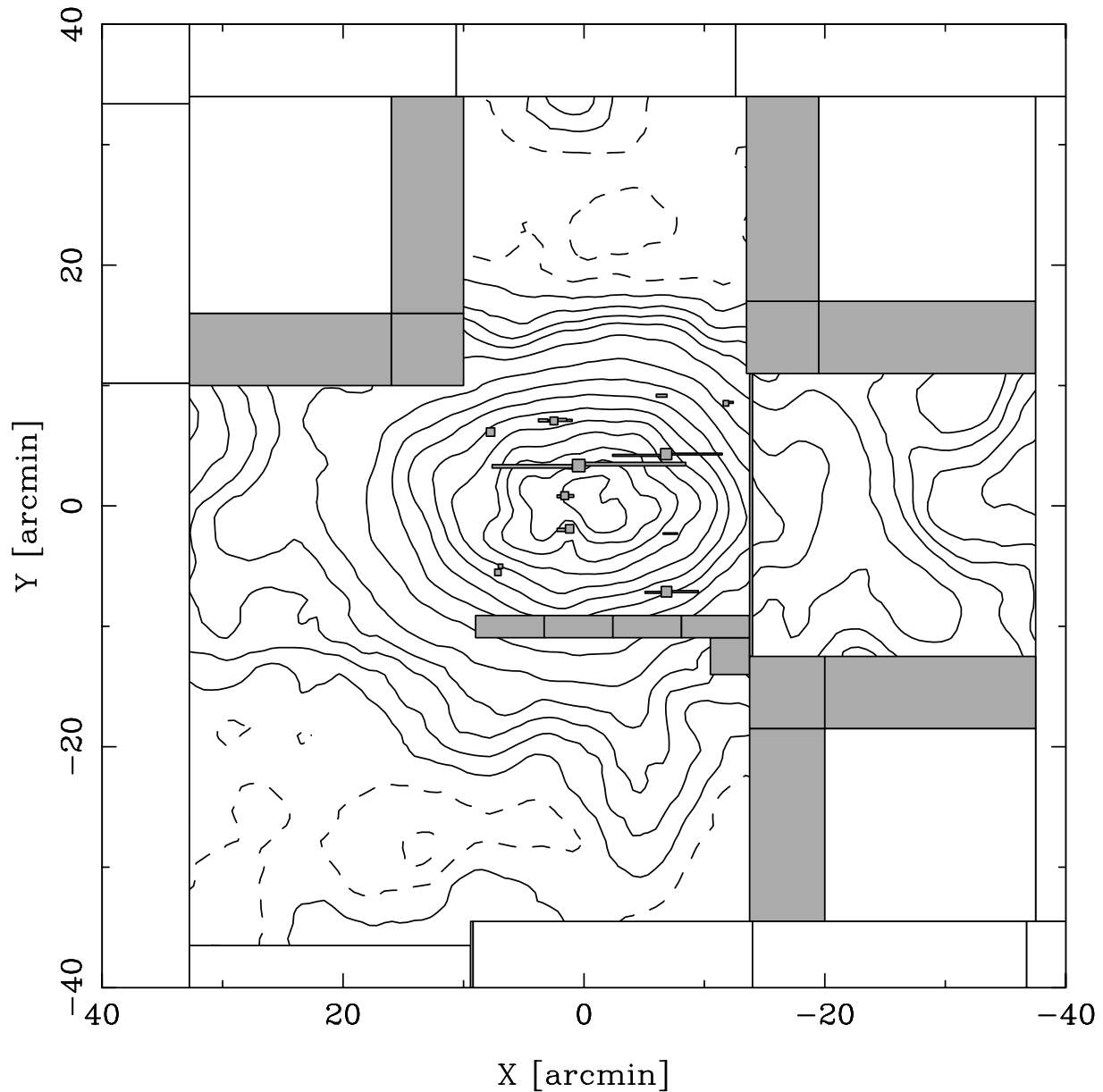
Fig. 6.—Isopleths for a smoothed surface density map of Draco using the "in" sample of objects. Dashed contours correspond to values below the background. The lowest contour levels are 0, ±1, ±2, 3, 4, and 5 σ from the background, where σ is the uncertainty of the smoothed density for locations in the map with densities near background. The spacing between the levels of the higher contours is 3 σ, where σ now is the uncertainty in the density at the value of the lower contour. The contour levels from lowest to highest are 1.145, 1.295, 1.446, 1.597, 1.747, 1.898, 2.199, 2.886, 3.787, 4.970, 6.522, 8.560, 11.234, 14.743, 19.348, and 25.391 arcmin^{-2}. The gray and white areas contain no data; see the text for details.

artificial objects generated from a constant distribution function scaled to have the average surface density of the background fields. The artificial objects in gray regions in the figure are drawn from the adjacent regions with the same area and containing real objects. While filling holes in the data is required for kernel estimates of the surface density, the surface density within a kernel width of large regions of artificial data should be treated with caution.

4.2. Contour Plot of the Surface Density

Figure 6 shows contours of constant surface density for Draco. The kernel size [w in the kernel $1 - (r/w)^2$, where r is the radial distance from the object] for the pilot estimate is 3.'1, producing largest and smallest adaptive widths of 1.'5 and 9.'9, respectively. Approximately 90

objects are within the area of the adaptive kernel, yielding a fractional uncertainty in the density of 0.11. The solid contour lines represent values of the surface density above the adopted background density, whereas dashed lines represent values below. Contours are drawn at 0, ±1, ±2, 3, 4, and 5 σ from the background level, where σ is the fractional uncertainty in the density estimate times the background density. The contour levels at higher surface density are spaced by 3 σ, where now σ is the fractional uncertainty times the surface density at the previous contour. The actual contour levels are in the figure caption.

The position angle of the major axis of the innermost contour is different from those for the more distant contours. We show in § 4.4 that the statistical significance of this appa-

rent difference is very low, arguing that this difference is caused by the sampling uncertainty in the surface density estimate.

The contours also show an apparent lopsidedness: there seems to be a shoulder about 10′ to the east of the center and a steeper gradient on the north side of the galaxy than on the south side. We test for the statistical significance of asymmetries along the major and minor axes in § 4.5. We find that these asymmetries are either due to the sampling uncertainty (along the major axis) or problems with the photometry (along the minor axis).

Figure 6 shows that surface densities above background extend beyond 28′.3—the tidal radius determined by IH—along and close to the major axis, which confirms the results of IH, Od01, and ACMD that Draco extends beyond the IH tidal boundary. IH argued on the basis of an abrupt change in the slope of the outer parts of their radial profile that these stars are not gravitationally bound, whereas the other authors argued on the basis of the absence of such a change that they are bound. A map of surface density can reveal tidal debris if the outermost contours show an S-shaped distortion or extended tidal tails. Grillmair et al. (1995), Leon et al. (2000), and Odenkirchen et al. (2001b) have detected such features around Galactic globular clusters. The visibility of S-shaped distortions around a Galactic dSph is likely to be suppressed by our position nearly in the orbital plane with respect to the dSph. However, the line-of-sight projection of this debris could still introduce irregularities into the structure. The contours in Figure 6 do not show any obvious signs of tidal distortions or extended tidal tails. However, our data do not extend far enough to rule out the existence of tidally induced distortions in Draco.

The surface density is below background about 20′ to the north and about 25′ to the southeast of the galaxy at the 1–2 σ level. Such regions are expected from fluctuations caused by counting statistics. However, the surface density is also lower than background in these regions in a similar map constructed using the "out" sample. The surface density of objects classified as nonstellar in the Sloan Digital Sky Survey data in the vicinity of Draco (York et al. 2000) also show lower than average values in these regions. All of this evidence suggests that large-scale structure in the distribution of galaxies, which are not completely eliminated from our "in" sample, is at least partly responsible for the low surface densities. The surface density of galaxies is lower in the southeast region than in the north region, whereas Figure 6 shows the reverse. We think that the large photometric uncertainties in the N1 field compared with our other fields have scattered more stars from the "in" sample into the "out" sample, thus reducing the measured surface density (see the discussion in §§ 2.2 and 3.2). This spuriously low surface density is likely responsible for the steeper density gradient seen on the north side of Draco compared to the south side.

4.3. *Center and Position Angle*

If the distribution of stars in Draco were not symmetric, then the center of Draco would depend on the method used to measure it. The first two methods employed in this study use a minimum of assumptions to find the center of Draco from the "in" sample of stars in the C0 field.

The first method finds a center of symmetry for Draco by using a mirrored autocorrelation of the one-dimensional distribution of stars in either the X- or Y-direction calculated in a sliding window 20′ wide in X and 14′ wide in Y. This method yields a center at $X = -0′.28$ and $Y = 0′.11$. Varying the size of the sliding window implies that the uncertainties in these positions are on the order of 0′.1.

The second method finds a center that minimizes the fractional rms scatter in the number of stars in the four quadrants of a circular aperture about their mean. The radius of the aperture equals the shortest distance between its center and the nearest edge of the C0 field. This method aligns the boundaries of the four quadrants with the major and minor axes of Draco, thus it also yields the position angle of the major axis. The resulting center is at $X = 0′.16 \pm 0′.18$ and $Y = 0′.15 \pm 0′.12$, and the position angle of the major axis is $90°.6 \pm 4°.6$. The uncertainties come from 1000 bootstrap determinations of the center and position angle. Each determination draws a sample of the same size as the original sample from the original sample with replacement.

4.4. *Do Ellipticity, Position Angle, and Center Depend on Semimajor Axis?*

With the assumption that the contours of constant projected density are ellipses, fitting ellipses gives another determination of the center and position angle of the major axis along with the ellipticity. The variation of these quantities with the length of the semimajor axis is an indication of the presence of asymmetries. Figure 7 shows the dependence of the ellipticity (e), the position angle (P.A.), the X-coordinate of the center (X_c), and the Y-coordinate of the center (Y_c) on the semimajor axes (a) of ellipses fitted to the estimate of the surface density described in § 4.2 and shown in Figure 6. The best-fit ellipse has the minimum rms fluctuation in the surface density measured at 360 points equally spaced in arc length around the ellipse. Each triangle in Figure 7 represents the value of the structural parameter determined from the fit to the actual sample. The corresponding square and its associated error bar represent the mean value of the structural parameter determined from 1000 bootstrap simulations and the rms scatter around this mean, respectively. The smallest value of the semimajor axis fitted is set by the minimum kernel width, and the largest by the presence of gaps in the data.

Figure 7a shows that the ellipticity, e, does not vary significantly with semimajor axis. The weighted average value of e is 0.331 ± 0.015, and the total χ^2 is 1.4. The uncertainties used to calculate these quantities come from the bootstrap experiments. Approximately only every other point is independent because of the smoothing. However, the value of χ^2 per the smaller true number of degrees of freedom is still less than 1, which shows that the variation in e is not significant.

This conclusion is strengthened by results from Monte Carlo simulations of fitting ellipses to the density field of a symmetric model of Draco. The model is the power law with a core used by Kleyna et al. (1998) and has $e = 0.29$, P.A. $= 88°$, $X_c = Y_c = 0′$, a core radius of 17′.7, and a power-law exponent of 4.1. The values for the last two parameters come from fits to our data. Each realization of the model is smoothed adaptively in the same way as the real data. Figure 8 shows the mean values of e, P.A., X_c, and Y_c from 1000 Monte Carlo experiments. The error bar is the rms scatter around the mean. Figure 8a shows that the mean e is biased upward to about 0.4 for a semimajor axis of 3′.0.
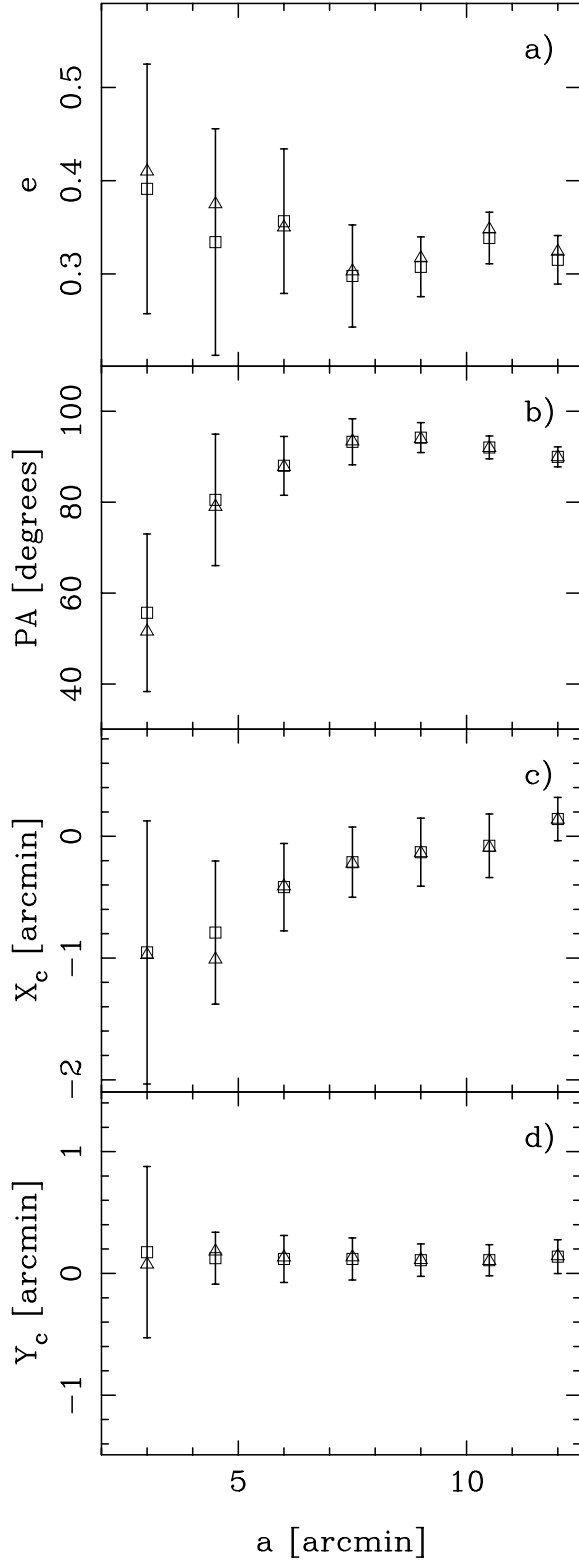
FIG. 7.—Dependence on semimajor axis, *a,* of (*a*) ellipticity, (*b*) position angle of the major axis, (*c*) *x*-coordinate of the center, and (*d*) *y*-coordinate of the center for ellipses fitted to the smoothed density map of Draco. A triangle represents the value of the structural parameter determined from fitting to the map shown in Fig. 6. A square and its associated error bar represent the mean value of the structural parameter and the rms scatter around the mean, respectively, determined from 1000 bootstrap experiments. Only approximately every other point is independent because of the smoothing in the density map.
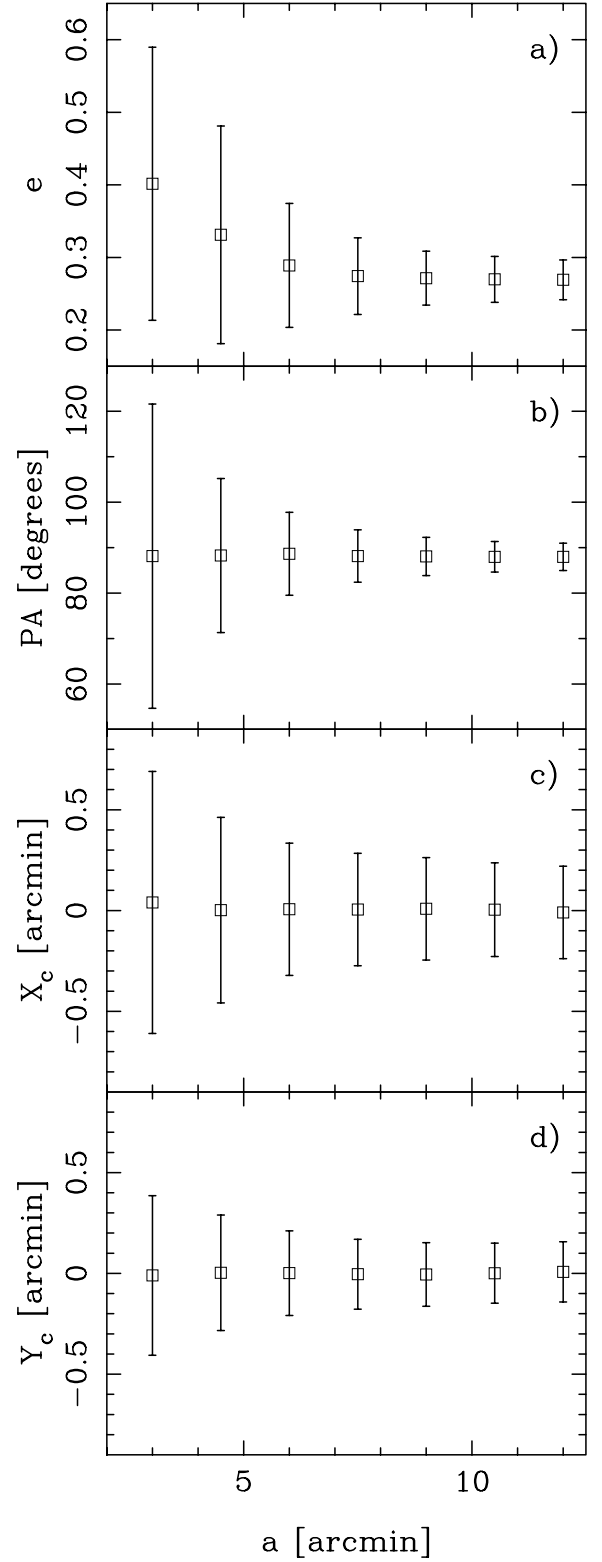
FIG. 8.—Dependence on semimajor axis, *a,* of (*a*) ellipticity, (*b*) position angle of the major axis, (*c*) *x*-coordinate of the center, and (*d*) *y*-coordinate of the center for ellipses fitted to the smoothed density map for a symmetric model of Draco. Each point and its associated error bar represent the mean and rms scatter around the mean, respectively, determined from 1000 Monte Carlo experiments.

Our fitted ellipticities for the real data show a very similar trend.

Figure 7b plots the position angle of the major axis, P.A., versus semimajor axis. The P.A. varies from $52° ± 17°$ at $a = 3.'0$ to $90.°0 ± 2.°2$ at $a = 12.'0$. The innermost point is about two standard deviations below the mean of the points at larger semimajor axes, implying a marginally significant change of P.A. The orientation of the surface density contours in Figure 6 also shows this change. Figure 8b shows that the rms scatter in the P.A. at a semimajor axis of $3.'0$ is large enough that statistical fluctuations can explain the change observed in the real data.

Figure 7c shows that X_c systematically increases with increasing semimajor axis. Figure 8c–8d shows that, on average, a symmetric model produces no such trends. The trend in the real data reflects a small asymmetry of the contours in Figure 6, as described in § 4.2. Section 4.5 tests the statistical significance of this apparent asymmetry and finds that it is not. The χ^2 for the X_c values about their weighted mean of $−0.'10 ± 0.'11$ is about 1 per degree of freedom, which also argues that the trend is not significant.

Finally, Figure 7d plots the Y-coordinate of the center, Y_c. There is no evidence for a dependence of Y_c on semimajor axis. The weighted mean of Y_c is $0.13 ± 0.06$.

4.5. Asymmetry

The contour plot of Draco depicted in Figure 6 shows an apparent "shoulder" about $10'$ to the east of the center, approximately along the major axis, and a steeper gradient beyond $10'$ from the center on the north side than on the south, approximately along the minor axis. The statistical significance of an asymmetry can be ascertained by measuring how often asymmetry can arise by chance from a symmetric model of Draco due to the finite size of the sample of stars.

Kleyna et al. (1998) defined an asymmetry statistic, $\beta = (d_1/d_2) − 1$, where d_1 and d_2 are the distances along the major or minor axis between the point of highest surface density and the points where the surface density has fallen by a factor of 2 and $d_1 > d_2$. A system is symmetric if $\beta = 0$, and it is asymmetric if $\beta > 0$. As defined, the β statistic can measure the asymmetry observed in our surface density map along the major axis. It cannot measure the observed asymmetry seen at a larger distance along the minor axis. However, the latter asymmetry is likely due to problems with the photometry in the N1 field discussed in §§ 2.2 and 3.2. Thus, we do not investigate this asymmetry along the minor axis.

Measuring β for the major axis by using the same projected density depicted in Figure 6 and a major axis position angle of $88°$ yields 0.24. Similarly, the value of β for the minor axis is 0.47. Monte Carlo simulations using the symmetric model described in the previous section give a larger value for β along the major axis 81% of the time and for β along the minor axis 69% of the time. Thus, the data show no evidence that Draco is asymmetric along either its major or minor axis.

4.6. Radial Profile

Figure 9 (top) plots the completeness-corrected surface density of objects from the "in" sample calculated in elliptical annuli versus the semimajor axes of the annuli. We calculate the area of the overlap between each annulus and the data by dividing the sky into $2.''8$ square bins and summing the areas of the bins whose centers are within the annulus and within the boundaries of our fields. The center of the annuli is at $X = −0.'10$ and $Y = 0.'13$. The annuli have an ellipticity of 0.33 and a major axis position angle of $91°$. The semimajor axis of an annulus is the average of the semimajor axes of the ellipses passing through the objects in the annulus. Each point has an error bar equal to the surface density divided by $\sqrt{N}$, where N is the actual (not completeness corrected) number of objects in the annulus. Figure 9 (bottom) plots the background-subtracted surface density using the value of 1.446 arcmin^{-2} from § 3.3. Here, the error bar includes the uncertainty in the background, 0.026 arcmin^{-2}, added in quadrature. The dashed line in each plot represents the surface density of the background. Table 3 lists the surface densities shown in Figure 9 (top) and their radii.

Figure 9 (top) shows that the surface density profile is approximately constant within a semimajor axis of $5'$ and decreases beyond. The profile flattens as it approaches the background surface density; however, it never becomes flat and continues to decrease to values below the background found from the fields at larger radii. The surface densities that are below background in the outermost four annuli are likely caused in part by inadequate corrections for incompleteness, as discussed in §§ 2.2 and 3.2, and in part by the statistical accident that the portions of these annuli sampled by our data are regions of true low surface density (see § 4.2).

Figure 10 shows the background-subtracted projected density profiles of Draco from IH, Od01, and this article. The open squares show the IH profile taken from their Table 3, with the first 24 points in the table binned by 2 and the remainder by 4. The error bars are based on counting statistics and the number of stars in each binned point. The triangles show the Od01 profile, where

TABLE 3
RADIAL SURFACE DENSITY PROFILE

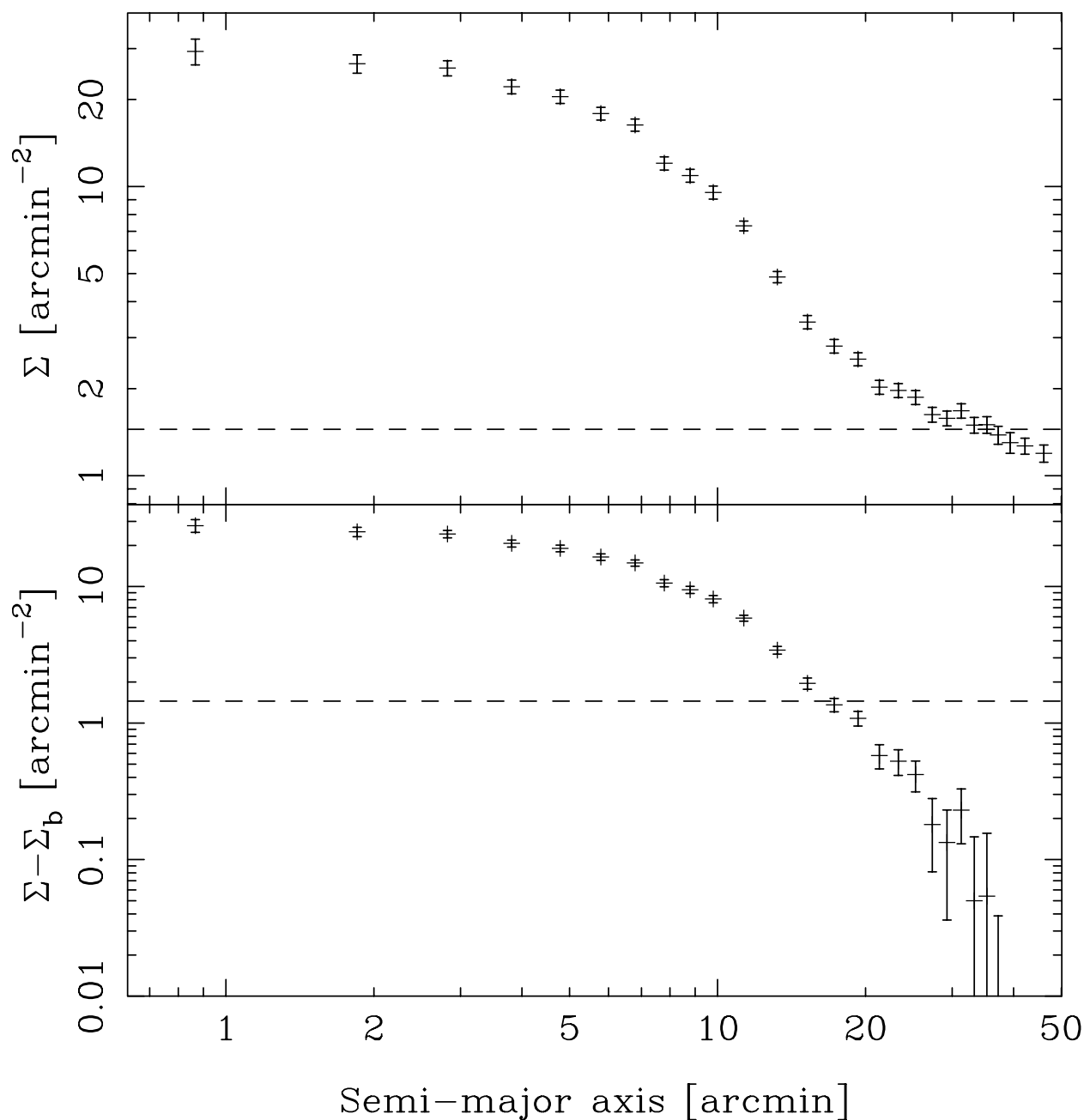| Semimajor Axis (arcmin)	Surface Density (arcmin^{-2})
1.514	27.47 ± 1.64
3.357	23.63 ± 0.96
5.307	19.03 ± 0.70
7.254	14.02 ± 0.50
9.290	10.19 ± 0.38
11.31	7.309 ± 0.285
13.23	4.863 ± 0.218
15.23	3.398 ± 0.182
17.26	2.807 ± 0.151
19.30	2.530 ± 0.131
21.33	2.024 ± 0.113
23.30	1.971 ± 0.109
25.27	1.866 ± 0.104
27.32	1.627 ± 0.096
29.28	1.580 ± 0.094
31.30	1.676 ± 0.096
33.26	1.496 ± 0.093
35.30	1.500 ± 0.099
37.21	1.383 ± 0.099
39.35	1.301 ± 0.107
42.17	1.267 ± 0.080
46.08	1.195 ± 0.082

FIG. 9.—Radial profile of Draco before (*top*) and after (*bottom*) subtracting the background. Table 3 lists the values of the surface density shown in the top, their uncertainties, and the radii.

the open triangles represent their S1 sample and the filled triangles represent their S2 sample. The filled squares show the profile in Figure 9 (*bottom*). The error bars for all of the profiles include the uncertainty in the background added in quadrature. The vertical normalizations of the four profiles make the innermost point of each equal to 1.

All four profiles in Figure 10 agree well up to a radius of about 20′. IH interpreted the apparent flattening of their profile beyond 20′ as evidence for extratidal stars. However, the IH profile has roughly as many points below background as above in this region, implying that the flattening is not statistically significant (Od01). In addition, the IH sample does not exclude galaxies, and so the error bars

shown are too small because the fluctuations in the surface densities of galaxies exceed those from Poisson statistics. Therefore, we think that the IH profile is consistent with those of Od01 and this article. The Od01 profile and that from this article agree well out to a semimajor axis of about 40′, and neither one shows an abrupt change of slope (a "break"). We conclude that none of the profiles show unambiguous evidence for tidal debris around Draco.

4.7. CMD *outside the Tidal Boundary*

Od01 report a tidal radius for Draco of 49.′5, based on fitting a King (1966) model, and ACMD report a tidal radius of 42′, based on a visual inspection of their radial surface
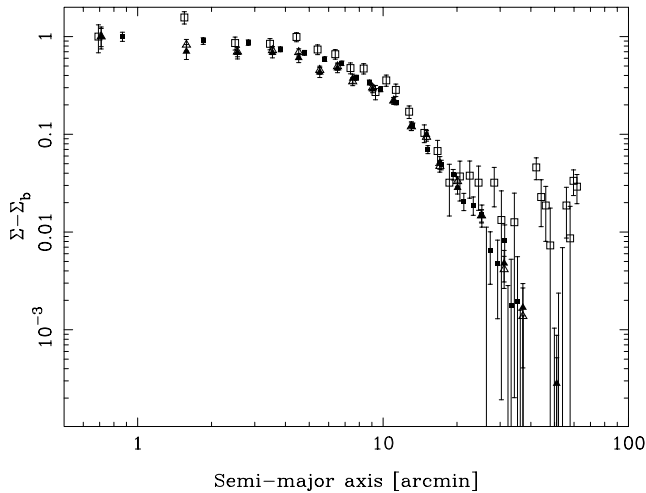
density profile. The difference between these two values reflects the difficulty of measuring the tidal radius. However, both studies demonstrate convincingly that Draco extends beyond the 28′.3 tidal radius found by IH. Od01 argue that this more extended profile explains the stars of Draco detected by P01 beyond the IH tidal boundary. To search for Draco stars at still larger radii, we plot a CMD for the objects inside and outside the Od01 tidal boundary, which is an ellipse with semimajor axis 49′.5 and position angle 88°, centered at $\alpha = 17^{\rm h}20^{\rm m}13^{\rm s}2$ and $\delta = 57°54'54''$ (J2000.0), which corresponds to $(-0′.73, -0′.19)$ in our standard coordinate system.

Figure 11 (*top*) is a CMD for the objects located inside the Od01 tidal boundary, and Figure 11 (*bottom*) is the corresponding plot for the objects outside. The CMD in the bottom shows no clear visual evidence of the principal sequences of Draco. This lack of visual evidence does not necessarily imply an absence of Draco stars beyond the Od01 tidal boundary. There could simply be too few Draco stars present to be noticeable in the CMD. Indeed, such a population is expected if the profile of Draco is an exponential, which has no limiting radius. Od01 and ACMD find that an exponential profile is a good fit to their projected density profiles.

5. SUMMARY AND DISCUSSION

The average center of Draco measured with three methods described in §§ 4.3 and 4.4 is at $\alpha = 17^{\rm h}20^{\rm m}18^{\rm s}1$ and $\delta = 57°55'13''$ (J2000.0). The uncertainty is about 0′.1 in both coordinates. This center is 40″ east and 19″ north of the center reported by Od01, a difference that is somewhat larger than that expected from the 25″ uncertainty in right ascension and 11″ uncertainty in declination of the Od01 value. However, the difference is smaller than twice the uncertainty and thus not statistically significant.

The position angle of the major axis of Draco is $90°.6 \pm 4°.6$, based on the objects within approximately 10′ of the center (see § 4.3). This value is in agreement with the $88° \pm 3°$ measured by Od01. Fitting ellipses to the
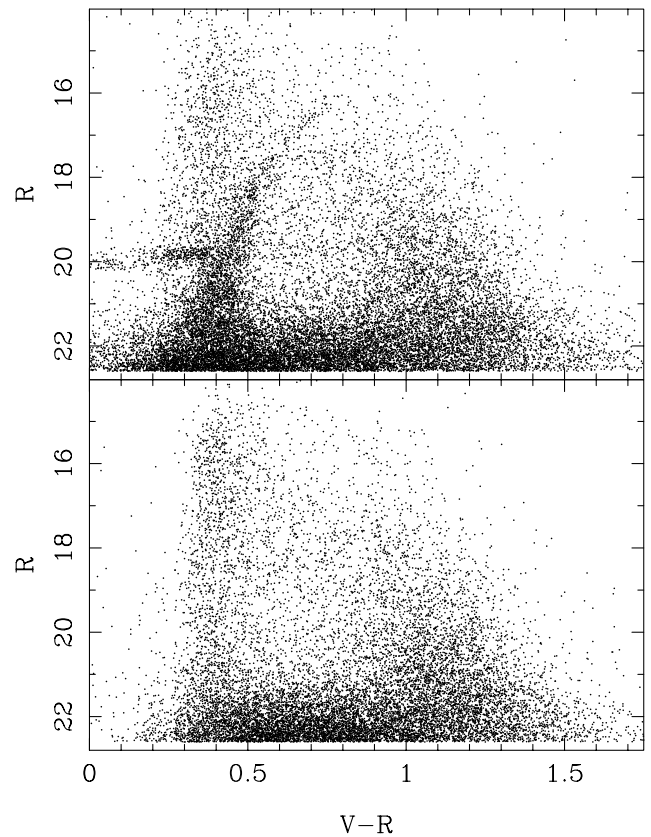
smoothed surface density, described in § 4.4, gives a range of position angles consistent with the above values. Od01 and this study find no evidence that the position angle of the major axis varies with semimajor axis.

The ellipticity of Draco, determined from the average of the values for the ellipses fitted to the smoothed surface density, is 0.331 ± 0.015. This average value is greater than the 0.29 ± 0.02 determined by Od01. Our value is less reliable because of the problems with the photometry and completeness corrections in the N1 field described in §§ 2.2 and 3.2.

Tidal debris projected onto a bound dSph can produce a small asymmetry in the surface density map (Mayer et al. 2001). A larger asymmetry might arise if the observed dSph consists primarily of unbound tidal debris (Kroupa 1997; Klessen & Kroupa 1998). The contours of the smoothed surface density in Figure 6 show an apparent "shoulder" about 10′ east of the center. We tested the statistical significance of the apparent asymmetry along the major and minor axes and found that both can occur by chance 81% and 69% of the time, respectively. Therefore, we find no compelling evidence for asymmetries in Draco, tidally induced or otherwise.

Figure 10 shows that the radial profile of Draco from this study agrees with the radial profiles from IH and Od01 within the uncertainties. The radial profile of Draco does not show evidence of an abrupt change or break in the slope. In addition, the CMD in Figure 11 does not show the principal sequences of Draco for the region beyond the Od01 tidal boundary, which is also about the last point in our radial

profile. Thus, we find no evidence that Draco is surrounded by tidal debris.

REFERENCES

Aaronson, M. 1983, ApJ, 266, L11
Aparicio, A., Carrera, R., & Martínez-Delgado, D. 2001, AJ, 122, 2524 (ACMD)
Armandroff, T. E., Olszewski, E. W., & Pryor, C. 1995, AJ, 110, 2131
Dejonghe, H., & Merritt, D. 1992, ApJ, 391, 531
Grillmair, C. J., Freeman, K. C., Irwin, M., & Quinn, P. J. 1995, AJ, 109, 2553
Irwin, M. J., & Hatzidimitriou, D. 1995, MNRAS, 277, 1354 (IH)
Johnston, K. V., Majewski, S. R., Siegel, M. H., Reid, I. N., & Kunkel, W. E. 1999a, AJ, 118, 1719
Johnston, K. V., Sigurdsson, S., & Hernquist, L. 1999b, MNRAS, 302, 771
Johnston, K. V., Zhao, H., Spergel, D. N., & Hernquist, L. 1999c, ApJ, 512, L109
King, I. R. 1966, AJ, 71, 64
Klessen, R. S., & Kroupa, P. 1998, ApJ, 498, 143
Klessen, R. S., & Zhao, H.-S. 2002, ApJ, 566, 838
Kleyna, J. T., Geller, M. J., Kenyon, S. J., Kurtz, M. J., & Thorstensen, J. R. 1998, AJ, 115, 2359
Kleyna, J. T., Wilkinson, M. I., Evans, N. W., & Gilmore, G. 2001, ApJ, 563, L115
Kroupa, P. 1997, NewA, 2, 139
Kuhn, J. R. 1993, ApJ, 409, L13
Kuhn, J. R., & Miller, R. H. 1989, ApJ, 341, L41
Leon, S., Meylan, G., & Combes, F. 2000, A&A, 359, 907
Mateo, M. 1998, ARA&A, 36, 435
Mayer, L., Governato, F., Colpi, M., Moore, B., Quinn, T., Wadsley, J., Stadel, J., & Lake, G. 2001, ApJ, 559, 754
Milgrom, M. 1983, ApJ, 270, 365
Monet, D., et al. 1998, USNO-A V2.0: A Catalog of Astrometric Standards (Washington: US Na. Obs.)
Moore, B. 1996, ApJ, 461, L13
Odenkirchen, M., et al. 2001a, AJ, 122, 2538 (Od01)
———. 2001b, ApJ, 548, L165
Oh, K. S., Lin, D. N. C., & Aarseth, S. J. 1995, ApJ, 442, 142
Olszewski, E. W., Aaronson, M., & Hill, J. M. 1995, AJ, 110, 2120
Piatek, S., & Pryor, C. 1995, AJ, 109, 1071
Piatek, S., Pryor, C., Armandroff, T. E., & Olszewski, E. W. 2001, AJ, 121, 841 (P01)
Pryor, C. 1994, in Dwarf Galaxies, ed. G. Meylan & P. Prugniel (Garching: ESO), 323
Pryor, C., & Meylan, G. 1993, in ASP Conf. Ser. 50, Structure and Dynamics of Globular Clusters, ed. S. G. Djorgovski & G. Meylan (San Francisco: ASP), 357
Schlegel, D. J., Finkbeiner, D. P., & Davis, M. 1998, ApJ, 500, 525
Sellwood, J. A., & Pryor, C. 1998, Highlights Astron., 11, 638
Silverman, B. W. 1986, Density Estimation for Statistics and Data Analysis (London: Chapman & Hall)
Smith, H. A., Kuhn, J. R., & Hawley, S. L. 1997, in ASP Conf. Ser. 127, Proper Motions and Galactic Astronomy, ed. R. M. Humphreys (San Francisco: ASP), 163
Stetson, P. B. 1987, PASP, 99, 191
———. 1992, in ASP Conf. Ser. 25, Astronomical Data Analysis Software and Systems, ed. D. M. Worrall, C. Biemesderfer, & J. Barnes (San Francisco: ASP), 297
———. 1994, PASP, 106, 250
van den Bergh, S. 2000, The Galaxies of the Local Group (Cambridge: Cambridge Univ. Press)
Webbink, R. F. 1985, in Dynamics of Star Clusters, ed. J. Goodman & P. Hut (Dordrecht: Reidel), 541
York, D. G., et al. 2000, AJ, 120, 1579